Journal of Alloys and Compounds, 185 (1992) 369–384
JALCOM 250

The hydrogen activation of $LaNi_5$

E. H. Kisi, C. E. Buckley and E. M. Gray
Division of Science and Technology, Griffith University, Nathan, Qld. 4111 (Australia)

(Received October 3, 1991; in final form January 22, 1992)

Abstract

Changes to the hydridable intermetallic compound $LaNi_5$ and its hydriding behaviour during the first few hydrogen absorption–desorption cycles (activation) have been studied. A number of bulk (manometric hydrogen content measurements, optical microscopy), structural (X-ray and neutron diffraction) and microstructural (scanning and transmission electron microscopy) techniques provide strong evidence that the major part of the observed reduction in hysteresis after activation is due to the formation of extended two-dimensional defects in the alloy. Evidence is presented that these defects also contribute to the observed increase in the rate of hydride formation after activation.

1. Introduction

Metals and intermetallic compounds which form hydrides often benefit from a pre-treatment known as activation [1]. In some this is merely a soak in H_2 to remove oxygen contamination from the surface. For others, however, there are far more complicated techniques consisting of cycling in H_2 at high temperatures (*e.g.* FeTi). $LaNi_5$ is said to activate easily [1] in terms of the resistance of the surface to hydrogen absorption. There are, however, other important changes to hydriding behaviour as a result of activation. In the following we consider activation to include all changes which occur as a function of the number of initial hydriding cycles or other pre-treatments given to the material before it becomes a stable hydrogen absorber.

On first exposing $LaNi_5$ to hydrogen, a number of marked changes occur in the material. Single crystals or polycrystalline aggregates are broken down (decrepitated) into powders of particle size 4–20 μm [2] by the 24% volume increase associated with the $\alpha \rightarrow \beta$ transition. The pressure of the so-called absorption plateau region of the pressure–composition (*P–C*) phase diagram is high (approximately 770 kPa at 25 °C) and the desorption plateau pressure (approximately 140 kPa at 25 °C) is much lower during the first absorption–desorption cycle. Hence there is a large pressure hysteresis during the first cycle. Subsequent absorptions occur at successively lower pressures and the associated desorption pressures are successively slightly higher, therefore exhibiting much reduced hysteresis. After approximately five cycles, the absorption plateau has stabilized at approximately 230 kPa (25 °C) and

0925-8388/92/$5.00

the desorption plateau at approximately 160 kPa (25 °C). The first absorption occurs very slowly but subsequent cycles proceed at a much greater rate. Taken together, these changes are the outward manifestations of activation in $LaNi_5$, and a sample which has attained stable plateau pressures by repeated cycling is said to be activated. Activation has no influence on the hydrogen storage capacity which remains constant but greatly reduces the pressure hysteresis.

X-ray and neutron powder diffraction peaks recorded from activated $LaNi_5$ exhibit strong anisotropic broadening [3]. Broadening is greatest in the (*hk*0) peaks while no broadening of (00*l*) peaks is observed. Mixed-index peaks have intermediate widths. This broadening has been analysed as a combination of particle size and "microstrain" broadening [3–7]. Strain estimates are all close to 0.7–0.8% whereas the particle size estimates vary from 1 μm spheres down to 80 Å×2500 Å needles.

Three possible mechanisms for activation are suggested by the above. These are (i) that decrepitation exposes large amounts of clean $LaNi_5$ surface which is then available for chemisorption and absorption at lower pressures; (ii) that the decrepitation reduces the diffusion distances, causing faster absorption and facilitating stress relaxation in the particles, thus decreasing the pressure of hydrogen absorption; and (iii) that defect creation (manifested as microstrains) provides easy diffusion paths and facilitates motion of the α–β interface through the alloy.

The major part of the $LaNi_5$ literature deals with *P–C* phase diagrams and crystal structure models. This paper reports on a comprehensive study of the formation of the activated state using manometric *P–C* measurements, X-ray and neutron diffraction, optical microscopy, scanning electron microscopy (SEM) and transmission electron microscopy (TEM) techniques.

2. Experimental details

2.1. Samples

A commercial $LaNi_5$ alloy (Research Chemicals, Phoenix, AZ, alloy #1241: 32.44 wt.%La or $LaNi_{4.93}$) received in lump form was used throughout this work. The grain size of the as-received material was quite large and single crystals up to 50 mm^3 could be isolated. Such crystals were used for *P–C* measurements and for surface analytical studies. In addition, crushed powders were prepared in a rotating hammer mill. These powders were sieved into their 54–106 μm, less than 53 μm and much less than 10 μm (ground severely in a mortar, SEM observations showed most particles to be in the range 0.1–2.0 μm with isolated larger particles up to 10 μm) fractions. Use was made of these powders in *P–C* measurements and for X-ray and neutron diffraction. In the following, X-ray and neutron diffraction samples are labelled X or N respectively followed by the number of hydriding cycles each has undergone.

2.2. Pressure–composition P–C *measurements*

P–C phase diagrams were recorded by a simple manometric technique in which a reference volume is filled to a selected pressure and a valve is then opened to a sample chamber of calibrated volume. The decrease (increase) in pressure in the combined reference–sample chamber allows the amount of absorbed (desorbed) hydrogen to be calculated. The system is constructed from Cajon VCR components of very low leak rate and is hence suitable for long-term measurements. The use of an electronic pressure transmitter reading from zero to 1 MPa and a predictive computer algorithm incorporating virial coefficients gives high-quality pressure data and well-controlled increments in the hydrogen content.

2.3. Microscopy

Unactivated and activated powders were set in epoxy resin and polished to a 1 μm diamond finish. These samples were examined in a metallurgical microscope, then carbon coated and examined in a JEOL JSM35CF (for SEM).

Ion-beam-thinned samples of unactivated $LaNi_5$ for TEM were prepared with some difficulty from single-crystal starting material. Single crystals, when activated, were found to produce activated powders which have a small fraction of particles fine enough to be examined in TEM. These samples were generally thick, heavily defected and not ideally suited to TEM study. Both activated and unactivated materials were examined on a JEOl 1200FX transmission microscope at 120 kV.

2.4. X-ray and neutron diffraction data

X-ray powder diffraction data were collected from unactivated and activated powders using a vertical Philips goniometer operated in Bragg–Brentano geometry with 1° divergence and receiving slits and a diffracted-beam Soller slit. Cu Kα radiation was used with a nickel diffracted-beam filter. Data from the coarser powder suffered some powder-averaging problems.

Neutron powder diffraction data were collected from 10° to 160° (2θ) in 0.1° steps at $\lambda = 1.893$ Å on an unactivated powder (N0) and a partially activated powder (N0.6) sealed in quartz fluorimeter tubes. These data were collected on the high resolution power diffractometer (HRPD) instrument at the Australian Nuclear Science and Technology Organisation Lucas Heights Research Laboratories [8]. High intensity data were collected from a fully activated powder (N10) on the D1A instrument at the Institute Laue–Langevin, Grenoble, operated at $\lambda = 1.509$ Å from 10° to 156° (2θ) in 0.1° steps. *In situ* $LaNi_5D_x$ data were also recorded, in the course of other work [9], from an activated powder with a small amount of unactivated material included (N5). The latter data were recorded with $\lambda = 1.500$ Å neutrons on the HRPD at Lucas Heights.

The Rietveld analysis program LHPM1 [10], an extensively modified version of DBW3.2 [11], was further modified to take into account the anisotropic peak broadening present in data from activated samples. These

modifications and their relationship to previous models for the broadening in $LaNi_5$ are given in the Appendix. This program was used for the analysis of all X-ray and neutron data.

3. Results

3.1. Pressure–composition phase diagrams

The progress of some typical activating hydrogen cycles is illustrated in Fig. 1(a) where *P–C* phase diagrams are plotted for the first, second and sixth cycles of a 54–106 μm powder at 30 °C. These data were recorded with 60–90 min waiting time between each pressure increment except for cycle 1 where times in excess of 1800 min were used. Most striking is the large drop in the absorption plateau pressure after the first cycle. Subsequent

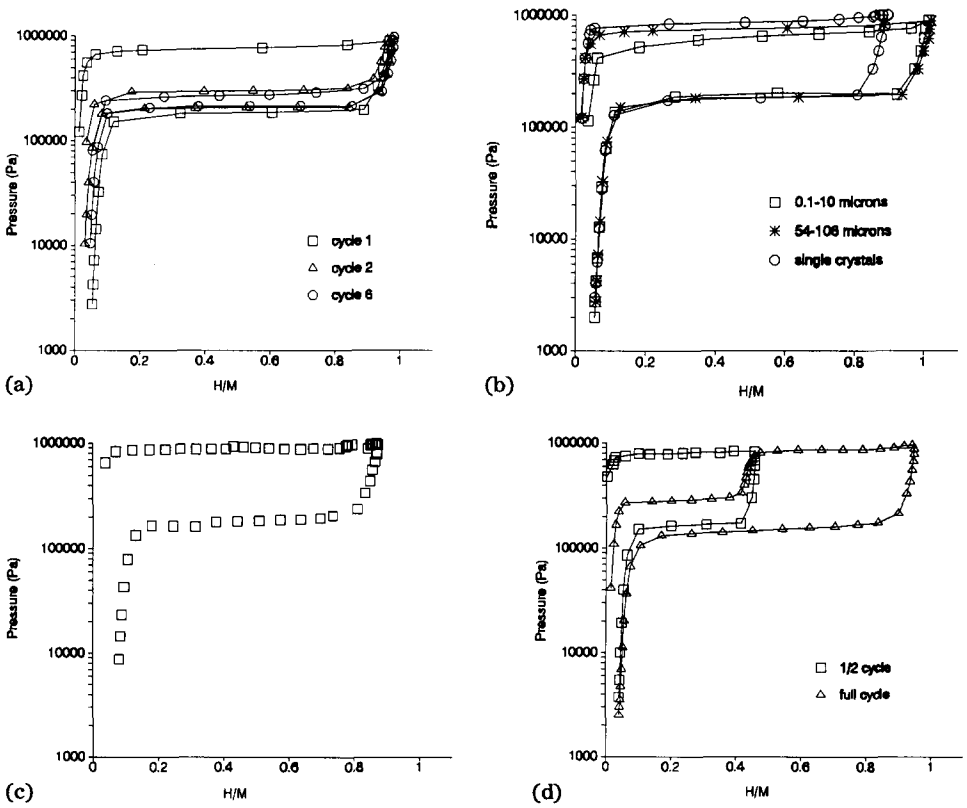

Fig. 1. *P–C* phase diagrams for (a) the first six cycles of a fresh (less than 106 μm) powder at 30 °C (□, cycle 1; △, cycle 2; ○, cycle 6), (b) the first cycle of fresh fine powder (□, 0.1–10 μm), coarse powder (*, 54–106 μm) and single-crystal (○) specimens, (c) the first cycle of a single-crystal $LaNi_5$ sample collected over a 2 month period (three days were allowed for the steady state to be achieved at each point on the absorption plateau and slightly less on the desorption plateau), and (d) an initially unactivated $LaNi_5$ sample given part of a hydriding cycle (□) followed by a complete cycle (△).

cycles have less dramatically decreased hysteresis until cycles 5 and 6 are virtually identical.

As a test of the influence of sample preparation technique, three samples prepared in different ways were given slow single hydriding cycles. The first was a very fine powder (mostly 0.1–2.0 μm with isolated larger particles up to a maximum of 10 μm) prepared by severe grinding with a mortar and pestle; the second was coarsely crushed (54–106 μm) in a rotating hammer mill; and the third was composed of small single crystals (1–8 mm^3). Their *P–C* diagrams are given in Fig. 1(b) and clearly the sample preparation has only a small influence on the high resistance of the virgin alloy to hydrogen absorption. The finest powder does have a reduced absorption plateau pressure but it remains high compared with the steady state absorption plateau pressure for fully activated material (*e.g.* cycle 6 in Fig. 1(a)). It is unclear whether the reduced hysteresis observed in the finest powder is due entirely to reduced particle size or whether the increased concentration of defects introduced by grinding has also contributed.

Since the absorption is slow during the first cycle, a cycle with very long waiting-time was performed (33.5 °C) to test the stability of the high first-absorption pressure of single crystals initially several millimetres in size. Here, 3 days was allowed for the steady state to be attained between pressure steps. The phase diagram (Fig. 1(c)) clearly shows that the absorption plateau pressure remained high throughout the 2.5 month duration of this cycle. Some major room temperature excursions occurred during this experiment, which in turn slightly influenced the sample temperature. These are visible as perturbations on the absorption plateau. There are no signs of any systematic change in the plateau pressure; in particular, there was no drift towards the plateau pressure for activated samples (approximately 280 kPa at this temperature).

Figure 1(d) is a *P–C* phase diagram for non-integer numbers of cycles. A 5.4 g sample was hydrided to an average hydrogen-to-metal ratio of 0.46. The sample was then desorbed and given a complete absorption–desorption cycle. Clearly that portion of the material converted to β phase in the part-cycle (now "soft" α) "remembers", and is converted much more easily the second time (first part of the complete subsequent cycle). When this portion of the sample is all β phase, the pressure climbs (existing β and residual "hard" α both take hydrogen into solid solution) until the plateau pressure for unactivated $LaNi_5$ is attained, whereupon conversion of hard α to β continues. The process is highly inhomogeneous with regions which have undergone the $\alpha \rightarrow \beta \rightarrow \alpha$ transition having such a thermodynamic (pressure) and kinetic advantage over regions never having formed β phase that no new material ("hard" α) is converted to β until all the "soft" α has undergone the transition for the second time. Similar behaviour has been reported by Flanagan and Biehl [12]. There the "starting state" of the material was assumed to be well-activated $LaNi_5$ and it was shown that annealing at temperatures between 450 and 1025 K caused an increase in the hysteresis of the first hydriding cycle completed after the anneal. The "split plateau"

halfway between the first and second cycle was loosely interpreted in terms of the influence of annealing on ΔG for the $\alpha \rightarrow \beta$ conversion. A more complete explanation is that the annealing has merely restored the alloy to the unactivated state (*i.e.* from cycle 6 to cycle 1 in Fig. 1(a)). Since the annealing temperatures involved were mostly well below those at which sintering of the activated powder would be expected, the annealing out of crystal defects is the only supportable mechanism for such behaviour. It therefore follows that the major part of the reduced hysteresis in activated $LaNi_5$ is due to the introduction of these same defects by the first passage of the α–β interface. In addition, the split-plateau behaviour for non-integral cycles, and indeed the reduced hysteresis after activation, strongly suggest that the passage of an α–β interface through the alloy is not only responsible for defect creation in virgin material but is greatly assisted by the presence of defects from previous passes. After approximately five cycles, the net rate of defect creation is zero and the pressures and rates have stabilized. The first (few) passage(s) of the α–β interface is (are) therefore intrinsically irreversible.

3.2. Microscopy

Optical and SEM examination revealed that activated $LaNi_5$ powders, whilst having a gross particle size in the range 4–20 μm [1], are in fact cracked up by hydriding into finer pieces in the 1–5 μm range which are still attached to each other.

TEM examination of unactivated $LaNi_5$ shows the alloy to be very perfectly crystalline. Figure 2(a) illustrates this in a wedge-shaped piece of crystal where pendellösung fringes are visible. The associated (00*l*) diffraction pattern is shown in Fig. 2(b). In contrast to this, activated powder particles are considerably defected. Figure 2(c) shows a poorly formed image of a series of dislocations and other defects in a thick piece of activated $LaNi_5$. Great difficulty was encountered in forming good images of activated samples because of lattice distortions and the thickness of the powder particles, but the result is nevertheless encouraging as it shows that TEM is possible in these materials, although further work on methods of sample preparation for TEM is required.

3.3. X-ray and neutron diffraction

Powder diffraction patterns collected from unactivated $LaNi_5$ in general show well-formed peaks of instrumental width. The finely ground powder used for *P–C* measurements showed isotropic line broadening, principally from small particle size but with a small strain component.

Both X-ray and neutron powder diffraction patterns from activated $LaNi_5$ have strong anisotropic peak broadening. Anisotropically broadened patterns have been analysed (see the Appendix) as a combination of isotropic particle size broadening and anisotropic "strain" broadening. The success of this approach is illustrated in Fig. 3 for the high intensity neutron pattern from sample N10. The refined parameters and R values are recorded in Table 1.

(a)

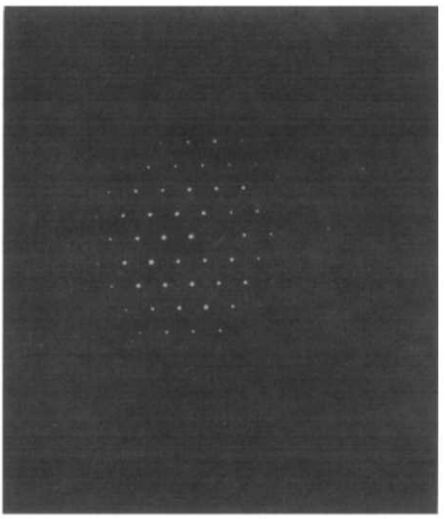

(b)

(c)

Fig. 2. (a) TEM image of a wedge-shaped crystal of unactivated $LaNi_5$ showing pendellösung fringes and a defect-free microstructure. (b) Selected-area electron diffraction pattern for the image in (a). (c) TEM image of defects in activated $LaNi_5$.

They provide a crystallite size estimate (isotropic) of 340 Å and a maximum r.m.s. microstrain of 0.0071 in the [*hk*0] directions. It is interesting to note that the difference profile has many features in common with fits reported for other size–strain models [7, 10], an effect which arises from the equivalence of the various approaches (see Appendix A).

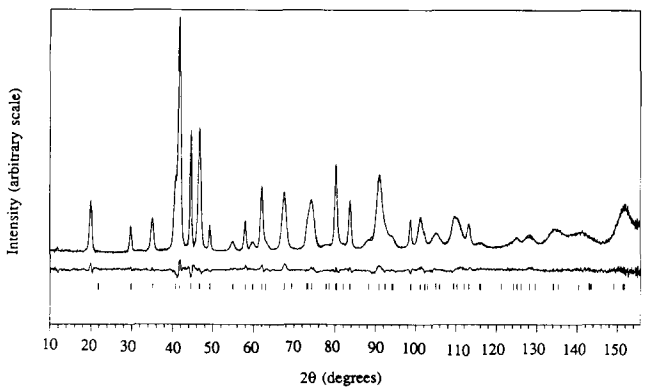

Fig. 3. Rietveld fit of the anisotropic line broadening model (eqn. (A6)) to neutron diffraction data from a well-activated $LaNi_5$ powder (N10). The data and the calculated profile are plotted as superimposed curves. Below are shown the difference profile $y_{i\,obs} - y_{i\,calc}$ and reflection markers as short vertical bars.

TABLE 1

Refined parameters for activated $LaNi_5$

Lattice parameters	a (Å)	5.0125(3)
	c (Å)	3.9873(2)
Thermal parameters	B_{La}	0.83(4)
	$B_{Ni(1)}$	0.88(2)
	$B_{Ni(2)}$	0.59(2)
Profile parameters	K	0.259(6)
	$\delta a/a$	0.970(6)
Zero shift 2θ	(deg)	0.031(3)
Total parameters	13[a]	
Reflections	59	
R factors	R_p	3.06%
	R_{wp}	3.59%
	R_B	1.56%
	R_E	2.26%
Goodness of fit		2.52

[a]Including a scale factor and four background parameters not recorded above.

The broadening is well advanced after one cycle as shown by the X-ray pattern in Fig. 4(a) from a powdered sample given one complete hydriding cycle. It is curious to note that single crystals activate (decrepitate) into powders with strong (00l) preferred orientation in contradiction to mechanically powdered samples which, when activated, show far less preferred orientation. This may be seen in Fig. 4(b) which shows a pattern collected from single crystals decrepitated into powder. Data were collected under the same conditions as in Fig. 4(a) except for shorter step counting times. Such behaviour is strongly suggestive that planar defects in the (00l) planes are associated with fracturing of single crystals. A sample which had been hydrided to a hydrogen-to-metal ratio of 0.6 was used to collect the data in Fig. 5(a).

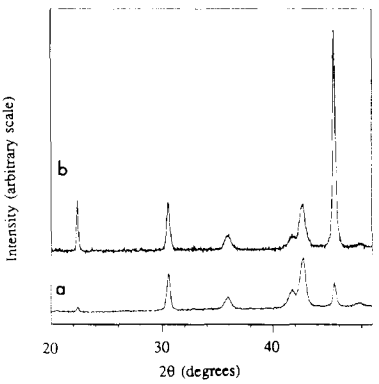

Fig. 4. X-ray diffraction scans from activated $LaNi_5$ from powdered starting material (curve a) and single-crystal starting material (curve b). Note the severe (0001) preferred orientation in the latter.

Broadening induced by activation has occurred; however, the mode of broadening is unusual. Unlike strain from cold working, or that from most other types of damage, where peaks of the same general shape broaden uniformly in response to increased damage, in the partially activated material the $LaNi_5$ peaks broaden non-uniformly, each peak having both a broad and a narrow component. Attempts to fit such peaks by a single function were unsuccessful. Also in Fig. 5 are compared a least-squares fit of a single Voigt function (width allowed to vary freely) with the (031) reflection of the X1 sample (Fig. 5(b)) and the fitting of two Voigt functions, one of instrumental width and the other with the same width as the (031) reflection of an activated sample (Fig. 5(c)). Clearly the calculated profile in Fig. 5(b) does not fit and that in Fig. 5(c) does. The same is true of the other lines in this pattern and also of other diffraction patterns from partially activated samples. This demonstrates simply that the material has been inhomogeneously defected. It consists of microregions which display fully developed anisotropic line broadening like the fully activated material (Fig. 3), and regions which are undamaged, showing no line broadening. Indeed a two-phase Rietveld refinement with undefected (narrow diffraction peaks) and defected (lines broadened according to eqn. (A6)) "phases" is readily carried out on such patterns. Such a refinement of the neutron data from this sample (N0.6) is also shown in Fig. 5(a) with the diffuse background (SiO_2 fluorimeter tube sample container) accounted for by fixed values taken from a pattern with no line broadening (N0 sample with identical sample container).

A small lattice parameter shift may be observed between the broad and narrow components of the N0.6 pattern (Fig. 5(a)) and is recorded in Table 2. Such shifts in the lattice parameters of the activated alloy have been reported before [5, 6] but never with the absolute internal consistency of having both materials present in the same sample. Also recorded in Table 2 are the *in situ* lattice parameters of the activated and unactivated portions

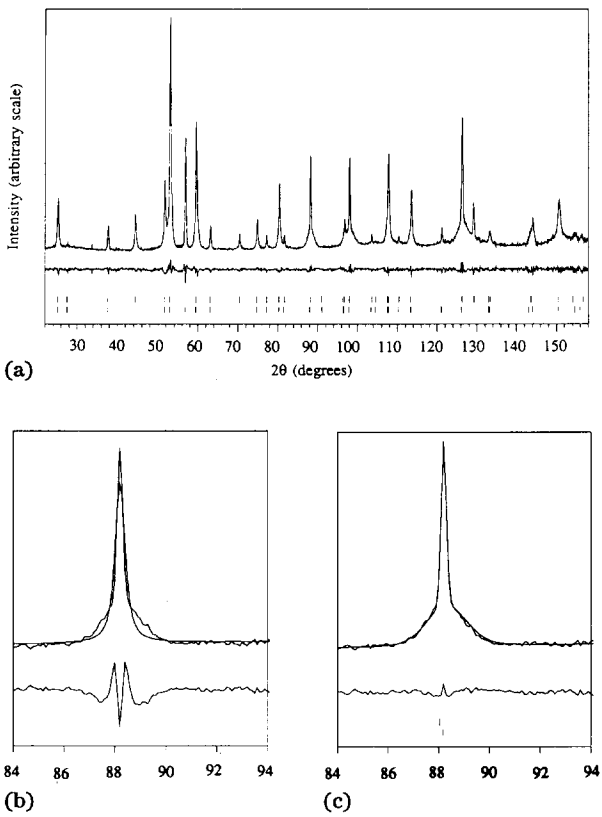

Fig. 5. (a) The neutron diffraction pattern from a sample hydrided to H/M=0.6 and then desorbed. Also shown is a Rietveld fit as a two-phase mixture of undefected $LaNi_5$ (narrow lines) and defected $LaNi_5$ (anisotropically broadened lines). The data and calculated profile are shown superimposed and the difference profile is shown below. The two sets of reflection markers are for the defected and undefected parts of the sample respectively. A small lattice parameter shift may be observed. (b) Least-squares fitting of the (031) reflection of sample N0.6 by a single Voigt function of variable width and (c) fitting by two Voigt functions, one of instrumental width and the other typical of (031) reflections in fully activated material (*e.g.* sample N10 in Fig. 3).

of sample N5 loaded into the α-phase region to a mean deuterium-to-metal ratio of 0.047. On reading these results, it is of interest to compare like with like, *i.e.* unactivated $LaNi_5$ with unactivated α-$LaNi_5D_x$ (column 1 of Table 2) and activated $LaNi_5$ with activated α-$LaNi_5D_x$ (column 2 of Table 2) as the two behave very differently. Unactivated $LaNi_5$ on absorbing small amounts of deuterium to become α phase expands only in the basal plane of the unit cell. Activated $LaNi_5$ expands by an equal fraction in both the a and c directions. Clearly irreversible changes have occurred in the alloy during activation which influence not only bulk properties (p_{abs}, p_{des} *etc.*) but also the fundamental crystal chemistry.

TABLE 2

Lattice parameters of $LaNi_5$ and α-$LaNi_5D_x$ (Å)

Compound	Parameter	Unactivated	Activated
$LaNi_5$	a	5.0215(1)	5.0141(5)
	c	3.9816(1)	3.9862(3)
α-$LaNi_5D_x$	a	5.0254(3)	5.0303(5)
	c	3.9816(3)	3.9998(2)

4. Discussion

4.1. Nature of the defects introduced by activation

Previous work on powder diffraction line broadening in $LaNi_5$ [2–6] has assumed the major contributing factor to be microstrains. The $\delta a/a$ approach used in the present work (Appendix) is just a simpler way of formulating strain broadening. The strain/size-broadening model of the activated alloy is deficient in many ways. There are few, if any, examples of strain broadening in homogeneous powders composed of fine single crystals. All are due to microstructural inhomogeneities such as crystal defects (dislocations, stacking faults, point defects), clustering or short-range order and compositional fluctuations. A proper physical model of the alloy must therefore centre on a knowledge of the specific defects causing the broadening. Many of the observations in this study suggest that the defects are two dimensional, in particular the preferred fracture of single crystals along (00l) planes and the anisotropy of diffraction line broadening. Stacking faults are a major two-dimensional defect type in layered structures and are a common cause of anisotropic broadening, but their existence in $LaNi_5$ has received scant reference in the literature. Lartigue *et al.* [5] have ruled out stacking faults on the assumption that extra selection rules for the broadened reflections would be generated if layers were sheared along a crystallographic direction. This is true in close-packed hexagonal materials for a $(1/3)[\bar{1}10]$ shear where (hkl) lines are broadened only when $h-k=3n+1$. Such faults are readily discounted in $LaNi_5$ because the large relative size of lanthanum would disrupt the d_{00l} spacing, giving rise to broadening of (00l), which is not observed. This is not the case for a $\frac{1}{2}[100]$ shear in the (00l) planes where a reasonable atomic model for stacking faults can be constructed. The resulting faults would be complex because of the ordered two-component structure of $LaNi_5$ but need not lead to any other selection rules (just as the $\delta a/a$ line broadening model used here has the correct (hkl) selectivity). TEM investigations are continuing in order to identify the defect structures causing the broadening.

4.2. Mechanisms for activation-reduced hysteresis

The absorption of hydrogen into activated $LaNi_5$ is much faster than into unactivated material. Therefore the activation appears to decrease the resistance of the alloy to the introduction of hydrogen. Two of the possible mechanisms for this rely on the fracturing which occurs in large lumps of

$LaNi_5$ hydrided for the first time. One is the creation of a large clean surface area by the break-up into a fine powder and the other is the reduced diffusion distances encountered by the hydrogen as the particle size is reduced. Both of these mechanisms would cause an acceleration of the first absorption as hydriding proceeds, which is not observed in practice. A third mechanism exists based on the existence of large numbers of defects in the material. These may speed up hydride formation by the provision of diffusion paths which have higher transport rates for hydrogen than those of the virgin material. Such a mechanism points to a two-dimensional defect type which would provide much greater access to interstitial sites in the alloy than either line or point defects and is considered to fit most closely all of the experimental observations to date.

The changes to the absorption and desorption pressures during the first few cycles reflect a decrease in the energy required (a) to put hydrogen into solid solution in the α phase and (b) to interconvert α phase and the β hydride. A clear indication of the first point is given by the slope of the absorption isotherm for the α phase. It has been observed that the α–β two-phase region of the phase diagram begins at the same hydrogen content in each cycle (Fig. 1). It follows that the slope of the α-phase isotherm, a quantity which depends on the interstitial site free energies [13], is reduced by the activation process. The second point is amply illustrated by the reduced hysteresis observed. Again there are three possible mechanisms, two reliant on specific surface area and particle size respectively. If any one of these were significant in the case of $LaNi_5$, then it would be expected that the first absorption of hydrogen into large lumps of $LaNi_5$ would occur at decreasing pressure as the lumps are broken up into fine powder and fresh surface is exposed. This is not the case as the *P–C* phase diagram shown in Fig. 1(c) illustrates. There is clearly no decrease in the absorption pressure as hydriding proceeds, indeed the pressure increases slightly along the α–β line (plateau) as is usually observed.

Additional evidence comes in the form of Fig. 1(d). Breakdown of lump or single-crystal material into fine powders by hydrogen absorption cannot occur without generating some fine α-phase particles in addition to the β phase. If activation results from a particle size or specific surface area effect, an experiment halted and recommenced would not return to the unactivated absorption pressure, as this one does, since much of the unactivated α phase would be present as small particles. That the major process causing this behaviour is defect related is amply illustrated by the diffraction work on partly activated material (Fig. 5). Furthermore, powders of very different sizes have been shown to have similar absorption plateau pressures. If size were the critical factor, the finer sample in Fig. 1(d) (which has a smaller particle size than the final size in activated powders) would be expected to have an absorption plateau typical of, or even lower than, that for activated material. If specific surface area were the ruling factor, the pressure would be expected to be lower because of the higher surface area. There is, in addition, the strong diffraction line broadening evidence. Crystallite size

estimates in the literature vary wildly from 80 Å to 1 μm. Since many of these reports have approximately the same quality of fit to the experimental data, crystallite size broadening is likely to be only a second-order effect in the presence of the strong strain broadening observed. The TEM work to date has confirmed the absence of defects in virgin $LaNi_5$ and their presence in activated material.

We are therefore led to conclude that the creation of a high density of defects is the major mechanism for the reduction in pressure hysteresis observed during the initial few hydriding cycles in $LaNi_5$. The defect generation has been shown here to be highly inhomogeneous when diffraction from samples with an incomplete first cycle is examined, but we are unable to decide conclusively whether the damaged regions constitute whole crystallites, others being undamaged, or whether the damaged and undamaged regions coexist within the same particle.

5. Conclusions

(1) The reduction in pressure hysteresis in $LaNi_5$ after the initial activation cycle(s) is associated with the creation of planar defects in the alloy which enhance hydrogen diffusion and assist the subsequent passage of the α–β interface on later hydriding cycles. Particle size effects have been eliminated as the primary factor in the activation process.

(2) The activation process, whereby the final defected state is induced in the material, occurs in a highly inhomogeneous fashion in which each microportion of the sample "remembers" how many times it has been hydrided.

(3) There is no way to prove, from our data, whether these microregions constitute whole crystallites, the inhomogeneity then being from particle to particle, or whether the damaged and undamaged regions of, say, sample N0.6 coexist within each particle.

(4) Whilst strain broadening models fit the X-ray and neutron data reasonably well, the underlying defects responsible for the broadening are yet to be identified. The presence of a high density of stacking faults on $(00l)$ planes with a $\frac{1}{2}[100]$ shear vector cannot be ruled out.

Acknowledgments

This work was carried out under National Energy Research Development and Demonstration Council grant 1429 with additional support from the Australian Institute of Nuclear Science and Engineering. The authors wish to thank Dr. R. L. Davis of the Australian Institute of Nuclear Science and Engineering for collecting the neutron diffraction patterns from samples N0 and N0.6 and Dr. C. J. Howard of the Australian Nuclear Science and Technology Organization for helpful discussions on diffraction line broadening. Thanks are also due to Dr. A. Hewat and Mr. J. Davies of the Institute

Laue–Langevin for assistance while collecting the N10 pattern. The SEM and X-ray diffraction work of Miss T. Kastrissios and Ion-beam thinning by Ms. J. Forester are gratefully acknowledged as are discussions with Associate Professor P. S. Turner, Dr. S. Myhra and Professor D. O. Northwood.

References

1 F. D. Manchester and D. Khatamian, *Mater. Sci. Forum.*, *31* (1988) 261–296.
2 H. H. Van Mal, *Philips Res. Rep., Suppl.*, *1* (1976) 1–102.
3 A. Pecheron-Guégan, C. Lartigue, J. C. Achard, P. Germi and F. Tasset, *J. Less-Common Met.*, *74* (1980) 1–12.
4 P. Thompson, J. J. Reilly, L. M. Corliss, J. M. Hastings and R. Hempelmann, *J. Phys. F*, *16* (1986) 675–685.
5 C. Lartigue, A. Le Bail and A. Percheron-Guegan, *J. Less-Common Met.*, *129* (1987) 65–76.
6 P. Thompson, J. J. Reilly and J. M. Hastings, *J. Less-Common Met.*, *129* (1987) 105–114.
7 K. Nomura, H. Uruno, S. Ono, H. Shimozuka and S. Suda, *J. Less-Common Met.*, *107* (1985) 221–230.
8 C. J. Howard, C. J. Ball, R. L. Davis and M. M. Elcombe, *Aust. J. Phys.*, *36* (1983) 507–518.
9 E. H. Kisi and E. M. Gray, submitted to *J. Alloys Comp.*
10 R. J. Hill and C. J. Howard, *Australian Atomic Energy Commission Rep. AAEC/M 112*, Lucas Heights, Australia, 1986.
11 D. B. Wiles and R. A. Young, *J. Appl. Crystallogr.*, *14* (1981) 149–151.
12 T. B. Flanagan and G. E. Biehl, *J. Less-Common Met.*, *82* (1981) 385–389.
13 T. B. Flanagan, in A. F. Andresen and A. J. Maeland (eds.), *Hydrides for energy storage, Proc. Int. Symp., Geilo, August 1977*, Pergamon, Oxford, 1978, pp. 43–59.
14 J. I. Langford, *J. Appl. Crystallogr.*, *11* (1978) 10–14.
15 H. P. Klug and L. E. Alexander, *X-Ray Diffraction Procedures for Polycrystalline and Amorphous Materials*, Wiley, New York, NY, 1974, and references cited therein.
16 M. M. Elcombe and C. J. Howard, *Mater. Sci. Forum*, *27–28* (1988) 71–76.

Appendix A: Rietveld analysis

The program LHPM1 [10], an extensively modified version of DBW3.2 [11], was used for refinements of X-ray and neutron diffraction data from uncycled materials (X0 and N0). The Voigt peak shape function [14], an analytical convolution of a gaussian and a lorentzian peak, was chosen for use throughout the analysis. It may be written as [10]

$$G_{ik} = \frac{C_1^{1/2}}{H_{Gk}} \pi^{-1/2} \mathrm{Re}[\omega(C_1^{1/2} X_{ik} + \mathrm{i} C_3 H_{Lk})] \quad \text{(A1)}$$

where G_{ik} is the intensity contribution of the kth reflection to the ith step, $C_1 = 4ln2, X_{ik} = (2\theta_i - 2\theta_k)/H_{Gk}, C_3 = 2^{-1.5}, H_{Gk}$ is the full width at half-maximum (FWHM) of the contributing gaussian, H_{Lk} is the FWHM of the contributing lorentzian, ω is the complex function and Re signifies its real part. The lorentzian component width is calculated from the function

$$H_{Lk} = \frac{180}{\pi} \frac{\lambda}{D} \sec \theta \quad \text{(A2)}$$

where $K=(180/\pi)(\lambda/D)$ is a refineable parameter and D is the mean (spherical) crystallite size. The gaussian component width is allowed to vary according to the Cagliotti function

$$H_{Gk}{}^2 = U \tan^2\theta + V \tan\theta + W \tag{A3}$$

where U, V and W are refineable parameters.

Isotropic microstrains in a material are commonly assumed [15, 10] to have a symmetric gaussian distribution about zero and are known to induce peak broadening with a tan θ dependence on diffraction angle. For a material giving strain-broadened lines we then have two terms, part of the instrumental breadth and the entire strain broadening, with a tan θ dependence. Being gaussian, they add in quadrature so that the U obtained during Rietveld refinement of the pattern may be partitioned as

$$U^2 = U_I^2 + U_S^2 \tag{A4}$$

in the isotropic case. Since the instrument parameter U_I is known from unbroadened samples, U_S is easily obtained. It is then possible, using the properties of gaussian distributions, to extract the isotropic r.m.s. strain as

$$\epsilon_{\text{r.m.s.}} = (U-U_I)^{1/2} \frac{\pi}{180} \frac{1}{4(2\ln 2)^{1/2}} \tag{A5}$$

The analysis of anisotropic broadening is more complex. The correct dependence of the width on hkl needs to be established. Early attempts [3] proposed a model for $LaNi_5$ where the angle between the normal to the plane under consideration and [00l] was the primary consideration and the angle to [hh0] provided a small second-order effect. Later efforts [5, 7] have assumed strain perpendicular to [00l] only combined with Fourier techniques for analysing the line shapes. Thompson *et al.* [6] used the standard approach (eqns. (A1)–(A5)) but using an approximate or pseudo-Voigt function (the analytic Voigt function was not widely available at the time of their work) and broadening the peaks anisotropically with the hkl functionality derived from the strain tensor for a hexagonal material.

We have adopted a related but much simpler approach. Since the (hk0) reflections are the most broadened and (00l) are unbroadened, a uniform δd_{hk0} can be easily simulated by a small change δa in the unit cell parameter a, leaving d_{00l} unchanged. Elcombe and Howard's technique [16] for modelling anisotropic broadening can therefore be applied to hexagonal $LaNi_5$. Here we allow a gaussian distribution of the unit cell parameter a about its mean position. The resultant expression for U_S in eqn. (A4) is

$$U_{S\,(hkl)} = \left[\frac{2(h^2+hk+k^2)/a^2}{(h^2+hk+k^2)/a^2 + l^2/c^2} \frac{\delta a}{a} \right]^2 \tag{A6}$$

where $\delta a/a$ is the FWHM of the gaussian distribution of the cell parameter and may be converted to $\epsilon_{\text{r.m.s.}\,(hkl)}$ by

$$\epsilon_{\text{r.m.s.}\,(hkl)} = \delta a/a \frac{1}{2(2\ln 2)^{1/2}} \frac{\pi}{180} \tag{A7}$$

Thus, by the addition of one parameter, fits of quality equal to or better than those of other techniques are achieved.

Because the Voigt function is a true convolution of a gaussian and a lorentzian function, its use is equivalent to the Fourier techniques. The major differences are in the order in which the necessary operations are carried out. Using the Voigt function, a convolution of two calculated functions is fitted by least squares to the raw data. Hence the whole operation is carried out in real space. In the Fourier techniques, the data is deconvoluted into two observed functions (a step involving the same assumptions concerning the functionality of crystallite size and strain broadening as in the Voigt function method) to which are fitted calculated functions. This operation is most often carried out in the Fourier space by means of the Fourier coefficients of the profile.